Pol. J. Environ. Stud. Vol. XX, No. X (XXXX), 1-10
DOI: *10.15244/pjoes/214017* ONLINE PUBLICATION DATE: 2026-07-02

Original Research

Preparation of Magnesium-Modified Dual-Sludge Biochar and Its Aqueous Phosphorus Adsorption Characteristics

Jingxi Tie[1], Yunhan Han[1], Mengjia Yan[1], Sihao Shao[1], Xiaohan Duan[2], Nan Zhang[3], Shuli Liu[1]*

[1]School of Environmental and Municipal Engineering, North China University of Water Resources and Electric Power, Zhengzhou, 450046, PR China
[2]Henan Vocational College of Water Conservancy and Environment, Zhengzhou, 450008, PR China
[3]Zhongzhou Water Holdings Co., Ltd, Zhengzhou, 450000, PR China

Received: 08 May 2025
Accepted: 05 November 2025

Abstract

In this study, magnesium-modified dual-sludge biochar (Mg@DSB) was synthesized using paper mill sludge, iron-based waterworks sludge, and magnesium ions as raw materials for the removal of phosphorus from the water. After characterizing the material, static adsorption experiments were conducted to evaluate its performance in phosphorus removal. The results demonstrate that within the pH range of 3 to 9, the adsorption capacity of Mg@DSB for phosphorus increases with rising pH levels. The adsorption process is well described by the pseudo-second-order kinetic model and the Langmuir isotherm. Thermodynamic analysis reveals that the adsorption of phosphorus by Mg@DSB is a spontaneous and endothermic process. The coexistence of Cl^-, NO_3^-, SO_4^{2-}, and sodium humate all significantly impaired the material's phosphorus uptake ($p<0.05$), with the three inorganic anions exerting a stronger suppressive effect than sodium humate ($p<0.05$). Nevertheless, increasing the concentration of any interferent did not lead to a further reduction ($p>0.05$). Mg@DSB enables highly efficient phosphorus removal from both the influent and effluent of a wastewater treatment plant. Mechanistic analysis further elucidates that the removal of phosphorus by Mg@DSB is driven by electrostatic adsorption and chemical precipitation.

Keywords: magnesium, paper mill sludge, iron-based waterworks sludge, dual-sludge biochar, phosphorus adsorption

*e-mail: liushuli@ncwu.edu.cn

Introduction

Phosphorus (P) is an essential element for plant growth [1], and is also widely used in industries such as electronics, daily chemicals, and metal processing. Therefore, P in the form of PO_4^{3-} enters water bodies through pathways such as phosphate mining, fertilizer manufacturing, agricultural production, food processing, waste treatment, and wastewater discharge, leading to eutrophication of water bodies and subsequently damaging aquatic ecosystems [2-4]. Thus, effective treatment of P-containing wastewater is highly necessary.

Currently, adsorption has proven highly effective for eliminating diverse aqueous pollutants, P included [5-8]. Among available adsorbents, biochar (BC) is especially prized for P removal because it is inexpensive, produced from abundant biomass, and requires only a straightforward manufacturing process [9, 10]. However, pristine BC surfaces are typically negatively charged, which creates electrostatic repulsion with PO_4^{3-}, resulting in unsatisfactory adsorption performance [11, 12].

Modification with Mg and Fe is widely used to enhance the P adsorption performance of BC [13]. Mg modification can improve P adsorption through the reaction between Mg^{2+} and PO_4^{3-}. For example, Liu et al. [14] modified peanut shell BC with $MgCl_2$ for P adsorption from water. The results showed that the Langmuir adsorption capacity for P of the pristine BC was 70.09 mg/g, while the maximum P adsorption capacity of the modified BC reached 150.16 mg/g.

Modification of BC with Fe^0 and Fe_3O_4 not only enhances the P adsorption performance of the material but also imparts magnetism, facilitating solid-liquid separation after adsorption. For example, as shown in the study by Ren et al., Fe^0 modified reed straw biochar achieved a maximum saturated aqueous P adsorption capacity of 95.2 mg/g [15]. Gong et al. prepared La-modified magnetic sewage sludge biochar via a one-pot hydrothermal method for P adsorption from water. The results showed that its monolayer saturated P adsorption amount was as high as 79.42 mg/g at 25ºC [5].

The papermaking industry produces a significant volume of sludge, yet effective resource utilization technologies for this waste remain limited. Given that paper mill sludge (PMS) is abundant in lignin, cellulose, and hemicellulose, it serves as an excellent feedstock for biochar production [16, 17]. In an effort to boost the P adsorption capacity of BC derived from PMS, we propose a novel approach utilizing iron-based waterworks sludge (IBWS) from water treatment plants as a source of iron to enhance its P adsorption. By blending these two types of sludge in an optimal ratio and subjecting the mixture to high-temperature pyrolysis under anoxic conditions, we aim to synthesize dual-sludge BC. Furthermore, we plan to further enhance its P adsorption performance through modification with magnesium ions. This innovative research not only addresses the challenge of waste management for both PMS and waterworks sludge but also offers a sustainable solution for P adsorption and removal. Our findings are expected to provide valuable insights and practical guidance for the resourceful utilization of these industrial by-products and the development of efficient P removal technologies.

Materials and Methods

PMS and IBWS used in this study were sourced from Xinmi, Henan Province, and Huludao, Liaoning Province, respectively. $MgCl_2 \cdot 6H_2O$ (Tianjin Kemiou Chemical Reagent Co., Ltd). A mixture was prepared by combining 1 g of IBWS, 3 g of PMS, and 25.1 g of $MgCl_2 \cdot 6H_2O$ in a 300 mL beaker, with mass ratios of IBWS:PMS: Mg^{2+} = 1:3:3. Subsequently, 100 mL of distilled water was added to each mixture. The mixtures were stirred at a speed of 400 rpm using a magnetic stirrer (Changzhou Surui Instrument Co., Ltd., SR-MS-6D) for 1 h, followed by a standing period of 11 h. The supernatant was then removed, and the residues were dried in a drying oven at 70ºC for 24 h, ground, and passed through an 80-mesh sieve.

The resulting mixtures were placed in a quartz boat inside a tube furnace (T-1200NT, Zhengzhou Tianzong Electrical Equipment Co., Ltd.). Nitrogen gas was introduced into the furnace at a flow rate of 300 mL/min to displace the air. After 30 min, the furnace was heated at a rate of 15ºC/min to 600ºC under a continuous nitrogen flow and maintained at this temperature for 90 min. After the reaction was complete, the furnace was allowed to cool to room temperature, with nitrogen gas continuing to flow for an additional 2 h. The final black product obtained was identified as magnesium-modified dual-sludge biochar (Mg@DSB). This material was ground again, passed through an 80-mesh sieve, and stored in a sealed container for further use.

Static Adsorption Experiment

Static P adsorption tests were conducted under two scenarios: (1) 0.04 g Mg@DSB was dispersed in 25 mL of synthetic P-containing wastewater whose pH was systematically varied; (2) 0.005-0.02 g Mg@DSB was contacted with 25 mL of either raw sewage or final effluent sampled from a municipal wastewater-treatment plant in Weihui, Henan Province.

For the static adsorption experiment, 0.04 g of Mg@DSB was added to a 50 mL flask containing 25 mL of simulated P-bearing wastewater with varying pH values. The flask was maintained at a constant temperature and placed in a shaker operating at a speed of 120 rpm. After shaking for a period of time, the mixture was removed and filtered through a 0.45 μm filter membrane. The residual P concentration in the filtrate was measured

using the molybdenum-antimony spectrophotometric method [18] at a wavelength of 700 nm, employing a spectrophotometer (752G, Shanghai INESA Scientific Instrument Co., Ltd.). Each experiment was performed in triplicate, and the average value was used for subsequent analysis to ensure data reliability.

Results and Discussion

Characterization

BET Specific Surface Area and Pore Information

As depicted in Fig. 1, in accordance with the classification of adsorption isotherms established by the International Union of Pure and Applied Chemistry (IUPAC), the Mg@DSB composite exhibits a Type IV isotherm, along with an H3 hysteresis loop. Typically, materials that display an H3 hysteresis loop are characterized by a lamellar particle structure. The BET specific surface area, total pore volume, and average pore size of this composite have been determined to be 44.446 m^2/g, 0.110 cm^3/g, and 9.910 nm, respectively (Table 1). These characteristics collectively indicate that Mg@DSB is a typical composite material featuring both micropores and mesopores [19, 20].

SEM Image

As depicted in Fig. 2a) and b), the morphology of Mg@DSB prior to adsorption reveals a surface that is densely populated with lamellar structures, which are irregular in shape and diverse in size. This observation aligns well with the material structure indicated by the H3 hysteresis loop. Following the adsorption process, these lamellar structures vanish, and the material surface becomes adorned with spherical particles. Consequently, the overall structure of the material takes on a more porous and fluffy appearance (Fig. 2c) and d)).

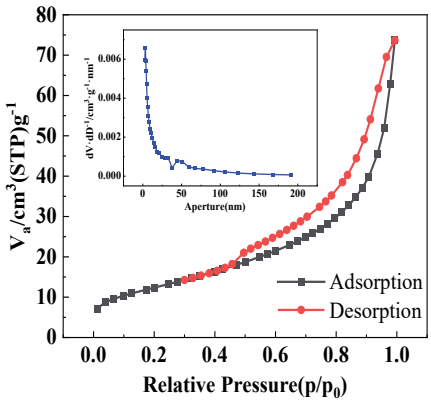

Fig. 1. N_2 adsorption-desorption curve of Mg@DSB.

Table 1. BET specific surface area and pore information of Mg@DSB.

Sample	S_{BET} (m^2/g)	Total pore volume (cm^3/g)	Average pore size (nm)
Mg@DSB	44.446	0.110	9.910

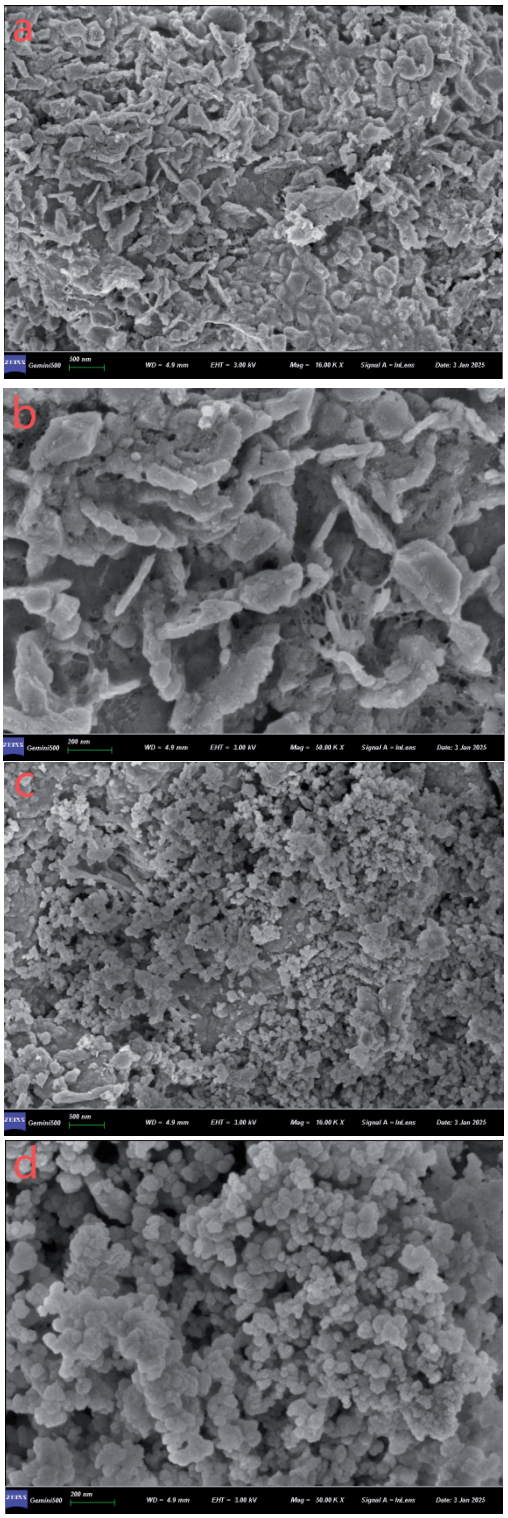

Fig. 2. SEM images before P adsorption a) 16K and b) 50K, and after P adsorption c) 16K and d) 50K.

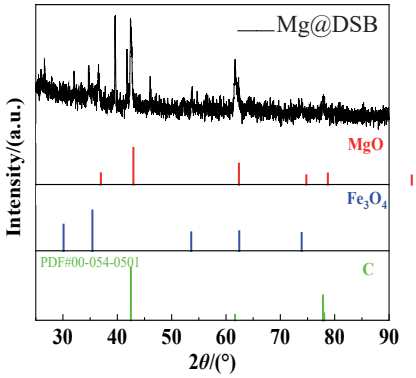

Fig. 3. XRD pattern of Mg@DSB.

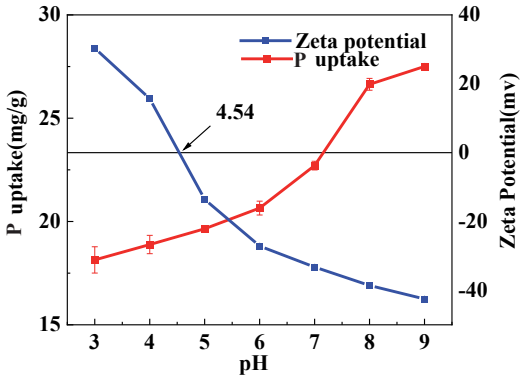

Fig. 4. P adsorption and zeta potential variation as a function of pH (C_0 = 50 mg/L, Time = 4 h, Temperature = 25ºC).

XRD Analysis

As shown in Fig. 3, the diffraction peaks at 42.46°, 61.62°, 77.92°, and 78.14° for Mg@DSB are attributed to carbon (C), corresponding to the crystal plane reflections at (020), (220), (301), and (002) [21]. The peaks at 30.08°, 35.48°, 53.66°, 62.32°, and 73.92° are assigned to Fe_3O_4, matching the crystal plane reflections at (112), (103), (132), (400), and (305) in [22]. Additionally, the peaks at 37.04°, 42.90°, 62.32°, 74.76°, and 78.74° are attributed to MgO, corresponding to the crystal plane reflections at (111), (200), (220), (311), and (222) as listed in [23].

Static P Adsorption

Effect of Starting Solution pH

Fig. 4 illustrates that as the solution pH rises from 3 to 9, the zeta potential of the material drops from 30.4 mV to -42.5 mV. The pH_{pzc} of Mg@DSB is around pH = 4.54. Below this value (pH<4.54), Mg@DSB's surface is positively charged, while above pH 4.54, it becomes negatively charged. Correspondingly, the adsorption of P from water by the material also increases significantly, ranging from 18.14 mg/g to 27.51 mg/g as the pH increases from 3 to 9.

At pH 2, P exists predominantly as H_3PO_4. As the pH increases to 4.54, P primarily adopts the form of $H_2PO_4^-$. This form readily engages in electrostatic interactions with the positively charged surface of Mg@DSB, enhancing the adsorption of P. However, when the pH rises from 4.54 to 9, the existing form of P shifts from $H_2PO_4^-$ to HPO_4^{2-}. In this higher pH range, the material surface acquires negative charges, and electrostatic repulsion between the negatively charged P species and the material surface would typically be expected to reduce adsorption. Yet, contrary to the expectation that adsorption would decrease due to electrostatic repulsion, the adsorption of P actually increases. This counterintuitive phenomenon is attributed to the enhanced precipitation of P as the aqueous pH values rise, a finding reported by Haddad et al. Their research revealed that P adsorption by B-Mg600 increased from 29.5 mg/g to 37.9 mg/g as the pH increased from 3 to 11 [24].

Adsorption Kinetics

Fig. 5a) illustrates P adsorption by Mg@DSB over time. It is evident that each adsorption process comprises an initial rapid adsorption phase, lasting for the first 30 min. This rapid phase is attributed to the abundance of active sites on the surface of Mg@DSB, which allows for efficient adsorption, achieving 43.0% and 46.5% of the total adsorption capacity, respectively. Subsequently, the reaction transitions into a slower stage as the active sites on the surface of Mg@DSB gradually become saturated and decrease in availability.

Adsorption kinetics is chiefly concerned with elucidating the dynamic interaction between adsorbents and adsorbates. By employing various adsorption kinetic models to fit experimental data, it becomes possible to predict the removal efficiency of the adsorbate, establish the temporal profile of residual adsorbate concentrations in solutions, and gain insights into the underlying mechanisms governing the adsorption process. In this study, the pseudo-first-order kinetic model, the pseudo-second-order kinetic model, and the Elovich kinetic model (Equations (1-3)) are utilized to simulate the removal process of P by Mg@DSB.

$$\ln(q_e - q_t) = \ln q_e - K_1 t \quad (1)$$

$$\frac{t}{q_t} = \frac{1}{K_2 \cdot q_e^2} + \frac{1}{q_e} \cdot t \quad (2)$$

$$q_t = \frac{1}{\beta} \cdot \ln(\alpha \cdot \beta) + \frac{1}{\beta} \cdot \ln t \quad (3)$$

where q_e (mg/g) and q_t (mg/g) are P adsorption at equilibrium and at time t, respectively. K_1 (1/min) and K_2 (g/mg·min) are the pseudo-first-order and pseudo-second-order rate constants, respectively. α (mg/g·min) and β (g/mg) are the initial adsorption rate

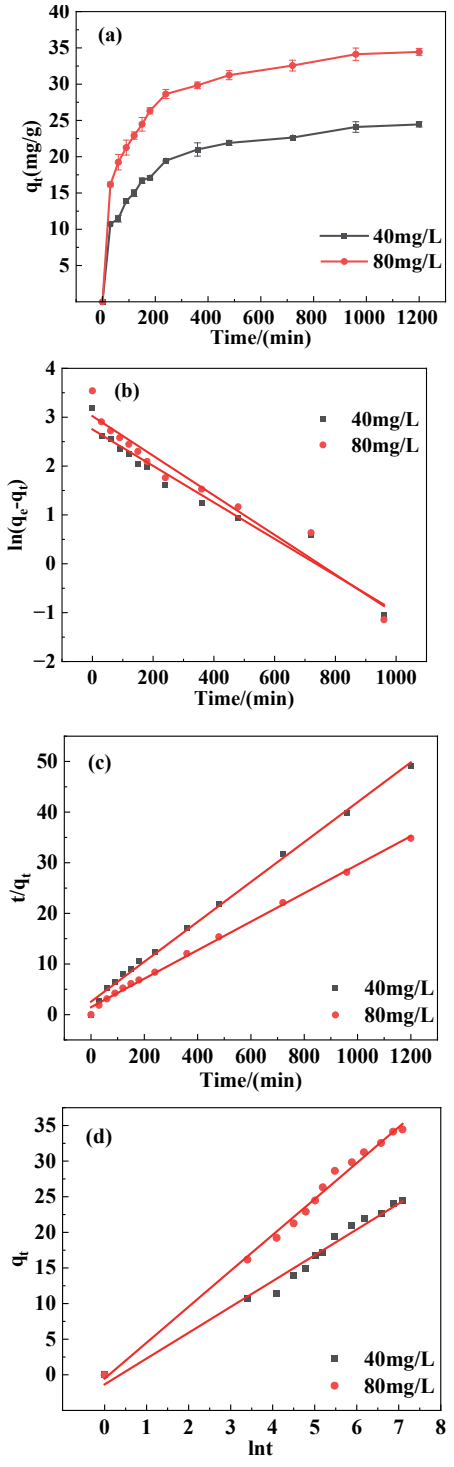

Fig. 5. a) Kinetic curves of P adsorption by Mg@DSB, b) linear fitting using the pseudo-first-order model, c) pseudo-second-order model, and d) Elovich model (pH = 7.0, Temperature = 25ºC).

and the desorption constant, respectively. The fitting results are shown in Fig. 5(b-d).

As shown in Table 2, under the two initial concentrations, the R^2 values of the pseudo-second-order kinetics are closest to 1. Meanwhile, the equilibrium adsorption capacities (q_e) obtained from the equation fitting, which are 25.39 mg/g and 35.53 mg/g for C_0 = 40 mg/L and 80 mg/L, respectively, are closer to the experimental values (24.4 mg/g and 34.4 mg/g). Therefore, the adsorption process follows pseudo-second-order kinetics. This also indicates that chemical adsorption plays a dominant role in this reaction process [25].

Adsorption Isotherms and Thermodynamic Studies

The relationship between the equilibrium adsorption capacity q_e and the equilibrium concentration C_e at three predetermined temperatures is illustrated in Fig. 6a). The results indicate that higher temperatures significantly enhance P adsorption. To elucidate the adsorption mechanism of P adsorption by Mg@DSB, the Langmuir and Freundlich models (Equations (4) and (5)) are applied to conduct linear fitting on the experimental data. The fitting results are presented in Fig. 6b) and c).

$$\frac{C_e}{q_e} = \frac{1}{q_m \cdot K_L} + \frac{C_e}{q_m} \quad (4)$$

$$\ln q_e = \ln K_f + \frac{1}{n} \cdot \ln c_e \quad (5)$$

Where q_e (mg/g) and C_e (mg/L) represent the amount of P adsorbed per unit mass of adsorbent and the concentration of P in the solution at equilibrium, respectively. q_m (mg/g) is the theoretical saturation adsorption capacity, K_L is the Langmuir adsorption constant, and K_f and n are the Freundlich adsorption constants.

The fitting parameters are shown in Table 3. It can be observed that under the three reaction temperatures, the R^2 values of the Langmuir model are all close to 1 and significantly higher than those of the Freundlich model. This indicates that the adsorption of P better conforms to the Langmuir model, suggesting that the adsorption process is a monolayer adsorption [25].

To further investigate the thermodynamic characteristics of the adsorption process, three thermodynamic parameters, including standard free energy change (ΔG^0), standard entropy change (ΔS^0),

Table 2. Fitting parameters of kinetic equations for the adsorption of P by Mg@DSB.

C_0 (mg/L)	Pseudo-first-order			Pseudo-second-order			Elovich		
	q_e	K_1	R^2	q_e	K_2	R^2	α	β	R^2
40	15.64	0.00373	0.950	25.39	0.0006	0.996	2.07	0.2593	0.978
80	20.49	0.00405	0.949	35.53	0.0006	0.997	3.91	0.1930	0.993

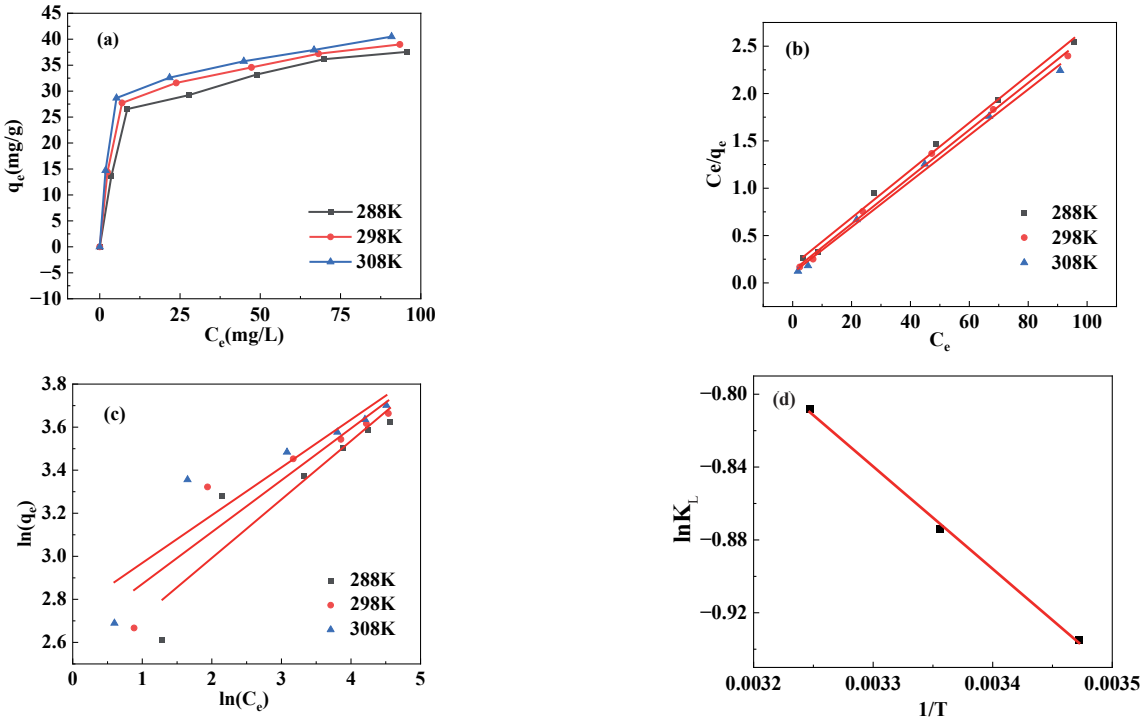

Fig. 6. a) Isotherms of P adsorption by Mg@DSB, b) the linear fitting results of the Langmuir model, c) the Freundlich model, and d) the relationship between lnK_L Vs. 1/T (pH = 7, Time = 24h).

Table 3. Parameters of the Langmuir and Freundlich models and thermodynamics.

T(K)	Langmuir			Freundlich					
	q_m	K_L	R^2	K_f	n	R^2	ΔG^0	ΔH^0	ΔS^0
288	36.98	0.137	0.995	15.591	4.502	0.815	-11.781	19.80	0.11
298	38.21	0.195	0.997	13.882	4.154	0.835	-13.064		
308	39.38	0.234	0.995	11.572	3.682	0.822	-13.970		

and standard enthalpy change (ΔH^0), were calculated using the following Equations (6-8).

$$\Delta G^0 = -RT\ln K_L \quad (6)$$

$$\Delta G^0 = \Delta H^0 - T \cdot \Delta S^0 \quad (7)$$

$$\ln k_L = \frac{-\Delta G^0}{RT} = \frac{\Delta S^0}{R} - \frac{\Delta H^0}{RT} \quad (8)$$

Where ΔG^0 represents the change in Gibbs free energy (kJ/mol), ΔS^0 denotes the standard entropy change (J/mol·K), and ΔH^0 indicates the standard enthalpy change (kJ/mol). The distribution coefficient, K_L, is the Langmuir adsorption constant (L/g). R is the universal gas constant (8.314 J/mol·K), and T represents the reaction temperature in Kelvin (K).

As indicated in Table 3, ΔG^0 values of the reaction are negative, and their absolute value grows larger as the temperature increases. This trend confirms that the adsorption of P occurs spontaneously [27]. Moreover, the positive values of ΔS^0 indicate that the adsorption process is driven by an increase in disorder and an enhancement of the stoichiometry at the solid-liquid interface. Meanwhile, the positive ΔH^0 suggests that the adsorption is endothermic in nature [28].

Effect of Coexisting Interfering Substances

P predominantly occurs in aquatic systems as oxyanions. Accordingly, we evaluate how three common inorganic anions (Cl^-, NO_3^-, and SO_4^{2-}) affect its adsorption. Because dissolved organic matter can also interfere, sodium humate is chosen as a model organic ligand, and its impact on the P-uptake capacity of Mg@DSB is quantified in parallel. Fig. 7 shows that all four interferents significantly reduced P removal ($p<0.05$). The inhibition is attributed to direct competition for surface-active sites among Cl^-, NO_3^-, and SO_4^{2-} and the humate anions released upon dissolution of sodium humate. Raising the concentration of any individual interferent does not further suppress P adsorption

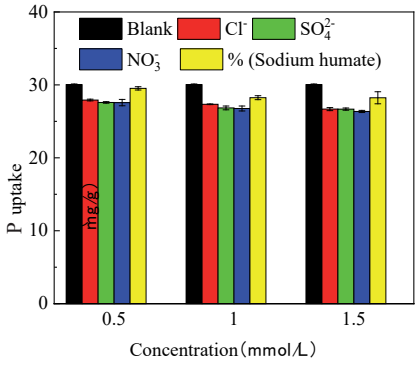

Fig. 7. Effect of coexisting ions on P adsorption (C_0 = 75 mg/L, Time = 4 h, pH = 7.0, Temperature = 25ºC).

(p>0.05). At every concentration, the three inorganic anions perform indistinguishably from one another (p>0.05), but sodium humate consistently produces the smallest decrease (p<0.05), underscoring its higher affinity for the Mg@DSB surface than the three inorganic anions.

P Elimination from Authentic Wastewater

To assess the real-world performance of P adsorption by Mg@DSB, influent and effluent samples were collected from a municipal wastewater treatment plant in Weihui, Henan Province, and used for P adsorption tests. Raw influent (RI), filtered influent (FI), and final effluent (FE) contain 3.53, 2.84, and 0.16 mg/L P, respectively. Fig. 8 shows that the specific P uptake from all three matrices declines as the composite dose increases, reaching a maximum of 13.31 mg/g for RI at 0.005 g. In contrast, P removal efficiency rises with dose: the lowest value (75%) is recorded for RI at 0.005 g, whereas complete removal (100%) is achieved for all samples at 0.02 g. These results confirm that the synthesized material efficiently removes P from authentic wastewater.

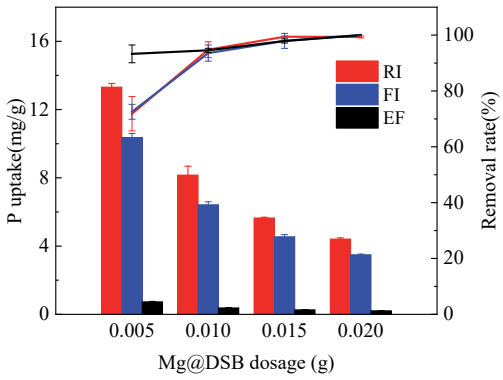

Fig. 8. P elimination from authentic wastewater by Mg@DSB (Temperature = 25ºC, Time = 4 h, pH = 7.2).

P Adsorption Mechanism Exploration

As previously discussed, when the solution pH falls below pH_{PZC}, the positively charged surface of Mg@DSB can effectively adsorb $H_2PO_4^-$ via electrostatic attraction. Meanwhile, the findings from the adsorption kinetics studies reveal that chemisorption is the predominant mechanism governing the adsorption process. Additionally, the results of adsorption isotherms and thermodynamic analyses demonstrate that P undergoes monolayer adsorption onto Mg@DSB, and this adsorption process is characterized as an endothermic reaction that occurs spontaneously.

The full XPS spectra depicted in Fig. 9a) reveal a significant change upon adsorption, with the emergence of a characteristic peak for P, thereby confirming that P has been effectively adsorbed onto the composite's surface. A closer examination of the high-resolution spectrum (Fig. 9b)) pinpoints the P 2p peak at 132.6 eV, which is assigned to the P-O [29].

As shown in Fig. 9c), the Mg 1s peak initially observed at 1304.3 eV prior to adsorption is attributed to Mg^{2+}, and the peak shifted to 1303.9 eV after P adsorption [30, 31]. This shift and the emergence of the new peak (1303.1 eV) in Fig. 9d) strongly suggest that a chemical reaction has taken place between Mg^{2+} and P, resulting in the formation of a precipitate. The reaction can be succinctly represented as Equation (9) [32]:

$$Mg^{2+} + HPO_4^{2-} \rightarrow MgHPO_4 \quad (9)$$

Fig. 9e) and f) present the high-resolution spectra of Fe 2p before and after the adsorption process. The peaks at 710.8 and 724.3 eV are indicative of Fe(II) [33, 34], whereas the peaks at binding energies of 714.8 and 727.8 eV are assigned to Fe(III) [35, 36].

Upon completion of the reaction, notable shifts in the peak positions of both Fe(II) and Fe(III) were detected. Specifically, the peak area of Fe(III) increased significantly from 17.54% to 28.32%, whereas the peak area of Fe(II) decreased considerably from 65.48% to 46.88%. This change is likely a result of Fe(II) being oxidized to Fe(III), which subsequently reacted with P, facilitating its adsorption [37, 38].

The primary reactions involved are represented as Equations (10-12):

$$4Fe^{2+} + O_2 + 2H_2O \rightarrow 4Fe^{3+} + 4OH^- \quad (10)$$

$$Fe^{3+} + 3H_2PO_4^- \rightarrow Fe(H_2PO_4)_3 \quad (11)$$

$$2Fe^{3+} + 3HPO_4^{2-} \rightarrow Fe_2(HPO_4)_3 \quad (12)$$

To sum up, the mechanism underlying the adsorption of P by Mg@DSB is primarily achieved through electrostatic adsorption and chemical precipitation.

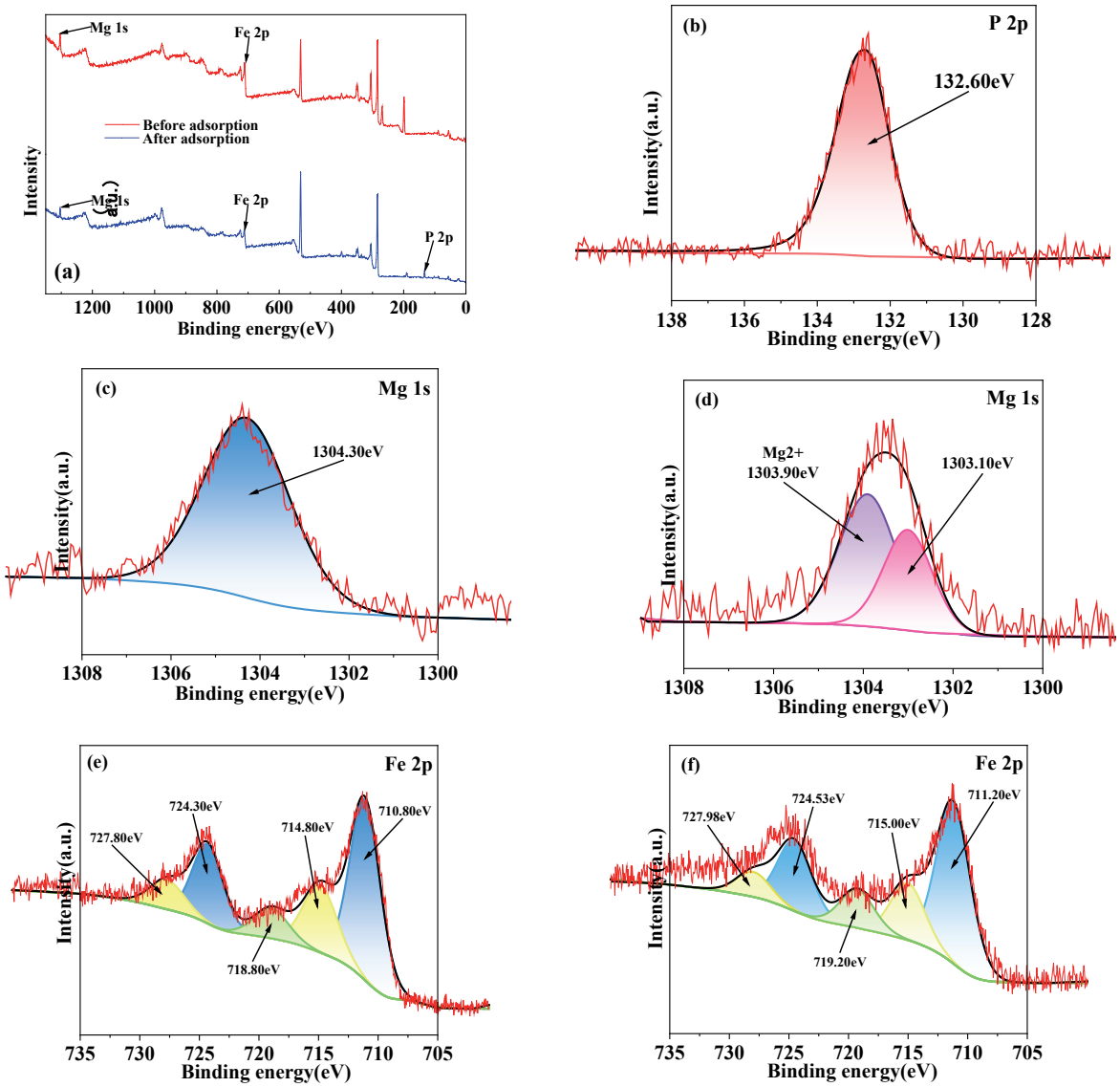

Fig. 9. a) Full XPS spectra of Mg@DSB before and after P adsorption, b) the detailed survey of P after P adsorption, c) Mg before and d) after P adsorption, e) Fe before and f) after P adsorption.

Conclusions

This study aims to achieve both the resource recovery of solid waste and the removal of P from water. To this end, we utilized paper mill sludge and water treatment plant sludge as raw materials, combined with magnesium ions as a modifier, to develop magnesium-modified dual-sludge biochar (Mg@DSB) for the adsorption and removal of P from water. The primary findings are summarized as follows: As the pH of the simulated P-containing wastewater is raised from 3 to 9, the adsorption capacity of the material for P increases significantly from 18.14 mg/g to 27.51 mg/g. Among the three kinetic models evaluated, the pseudo-second-order kinetic equation emerges as the most suitable descriptor of the adsorption process, thereby indicating that chemisorption is the predominant mechanism. The adsorption isotherm data closely align with the Langmuir equation, suggesting that monolayer adsorption is the primary mode of P uptake by the material. Thermodynamic analysis reveals that the adsorption of P by the material is a spontaneous and endothermic process. All four aqueous interferents markedly suppressed P adsorption ($p<0.05$), but raising their concentrations brought no additional significant decrease ($p>0.05$). Among them, the three inorganic anions diminished P removal more strongly than sodium humate ($p<0.05$). Mg@DSB can remove P from the influent and effluent of a sewage treatment plant efficiently. A comprehensive evaluation of the adsorption experiments and material characterization results indicates that P adsorption by Mg@DSB is mainly driven by electrostatic adsorption and chemical precipitation.

Acknowledgment

This research was funded by Henan Province Science and Technology Research and Development project (262102320117).

Conflict of Interest

The authors declare no conflict of interest.

References

1. KOESTOER R.H., LIGAYANTI T., KARTOHARDJONO S., SUSANTO H. Down-streaming small-scale green ammonia to nitrogen-phosphorus fertilizer tablets for rural communities. Emerging Science Journal. **8** (2), 625, **2024**.
2. ZUO Y., TIAN T., TIAN S., WAN L., XIAO B., LI L. Effects of fly ash modification on phosphorus adsorption of sludge-based biochar from aqueous solution. Journal of Material Cycles and Waste Management. **26** (6), 3893, **2024**.
3. QIAN H., ZHANG B., WANG Z., SONG X., JIANG H., YANG J., LIU J. La-doped CeO_2/rGO hybrid with high oxygen vacancy to enhance phosphorus adsorption by capacitive deionization. Separation and Purification Technology. **346**, 127515, **2024**.
4. CÔRTES P.R.B., BITENCOURT LEÃO M., REIS G.L.R., DE VARGAS D.D., MURILLO G.F., KÖHLER M.H., FERREIRA DE MATOS JAURIS C. Unraveling the phosphorus adsorption mechanisms in three-dimensional reduced graphene oxide materials. Langmuir. **40** (21), 11173, **2024**.
5. GONG W., QI C., HUANG L., TIAN Z., HUANG Z., TAO C., LIN H., GUO L., YU Z. Adsorption of phosphorus in wastewater by lanthanum-modified magnetic sewage sludge biochar. Desalination and Water Treatment. **320**, 100603, **2024**.
6. NAIK P.R., RAJASHEKARA V.A., MUDHULU S., CHANNEGOWDA M. Uranium removal from water by adsorption: a detailed characterisation and parametric study using nickel ferrite ($NiFe_2O_4$) nanoadsorbent. Environmental Pollutants and Bioavailability. **37,** 2515293, **2025.**
7. YIMRATTANABOVORN J., PHALAPHAI M., NAWONG S. Pulsed-bed column adsorption for triclosan removal using macadamia nut shell activated car-bon. Civil Engineering Journal. **10**, 1645, **2024**.
8. OBESO J.L., FLORES C.V., VILTRES H., MACHÍN-GARRIGA A., GUTIÉRREZ A.G., LEYVA C. High-performance adsorption of bisphenol A (BPA) from water: A comparison of Al-based MOF materials. Colloids and Surfaces A: Physicochemical and Engineering Aspects. **726**, 137813, **2025**.
9. WIJITKO S., SRIBURI T., KRUTNOI L. Taking advantage of disposal bamboo chopsticks to produce biochar for greenhouse crop cultivation. Emerging Science Journal. **8** (3), 917, **202**4.
10. WANG Z., YE X., YANG J., ZHANG Y., NAN Z., WANG Y., HUANG Y., WANG W. Boosting the phosphorus uptake of $La_2(CO_3)_3{\cdot}8H_2O$ based adsorbents via sodium addition: Relationship between crystal structure and adsorption capacity. Progress in Solid State Chemistry. **76**, 100496, **2024**.
11. XIANG S., CHU M., GONG C., FANG B. Adsorption Performance and Mechanism of Phosphate in Water by Magnesium Oxide-Corncob Biochar. Journal of Environmental Engineering. **149** (9), 04023053, **2023**.
12. HAGHIGHI MOOD S., AYIANIA M., CAO H., MARIN-FLORES O., MILAN Y.J., GARCIA-PEREZ M. Nitrogen and magnesium Co-doped biochar for phosphate adsorption. Biomass Conversion and Biorefinery. **14** (5), 5923, **2024**.
13. LUO D., WANG L., NAN H., CAO Y., WANG H., KUMAR T.V., WANG C. Phosphorus adsorption by functionalized biochar: a review. Environmental Chemistry Letters. **21** (1), 497, **2023**.
14. LIU X., ZHOU W., FENG L., WU L., LV J., DU W. Characteristics and Mechanisms of Phosphorous Adsorption by Peanut Shell-Derived Biochar Modified with Magnesium Chloride by Ultrasonic-Assisted Impregnation. ACS Omega. **7** (47), 43102, **2022**.
15. REN L., LI Y., WANG K., DING K., SHA M., CAO Y., KONG F., WANG S. Recovery of phosphorus from eutrophic water using nano zero-valent iron-modified biochar and its utilization. Chemosphere. **284**, 131391, **2021**.
16. WANG Q., XIONG J., SONG Q., SHAHEEN S.M., SALEM H.M.S., MOHAMED I., MAJRASHI A., WANG S., RINKLEBE J., YAO Z., QI W. Preparation of nitrogen-enriched Fe-doped porous biochar using the catalytic pyrolysis of paper mill sludge. Biomass Conversion and Biorefinery. **14** (13), 13877, **2024**.
17. KUMAR V., VERMA P., DE FREITAS F.A., SRIVASTAVA P.K., VASHISHTH A., AMéRICO-PINHEIRO J.H.P. A critical review on biofuels generation from pulp-paper mill sludge with emphasis on pretreatment methods: renewable energy for environmental sustainability. BMC Environmental Science. **2** (1), 2, **2025**.
18. HE K., LI X., DONG L. The effects of flue gas desulfurization gypsum (FGD gypsum) on P fractions in a coastal plain soil. Journal of Soils and Sediments. **18** (3), 804, **2018**.
19. THOMAS S., UMAR A., YUNARTI R.T., BAKRI R., PUTRA B.R., WAHYUNI W.T., ARIFUTZZAMAN A., AROUA M.K., KHALIL M. Mesoporous metal oxide via nanocasting: Recent advances on types of templates, properties, and catalytic activities. Materials Today Communications. **40**, 110152, **2024**.
20. HUANG Y., LI S., CHEN J., ZHANG X., CHEN Y. Adsorption of Pb(II) on mesoporous activated carbons fabricated from water hyacinth using H_3PO_4 activation: Adsorption capacity, kinetic and isotherm studies. Applied Surface Science. **293**, 160, **2014**.
21. SALAMUN N., NI H., TRIWAHYONO S., ABDUL JALIL A., KARIM A. Synthesis and characterization of Fe_3O_4 nanoparticles by electrodeposition and reduction methods. Malaysian Journal of Fundamental and Applied Sciences. **7** (1), **2011**.
22. DA COSTA ARAUJO J.F., NOGUEIRA DA SILVA AVELINO OLIVEIRA ROCHA G., RODRIGUES SILVA J.Y., RIBEIRO ROCHA J.V., FIGUEIROA BAKUZIS A., ALVES JUNIOR S. Fe_3O_4/ZIF-8-90 nanocomposite as a strategy for oncological treatment. ACS Omega. **10** (27), 2849, **2025**.
23. GUO Y., LI Z., LIU F., WANG S., CHEN F., YANG L., LI Z. Corrosion behavior of $CaO–Al_2O_3–SiO_2–MgO-Cr_2O_3$ slag on MgO refractory brick for smelting of chromite.

Journal of the European Ceramic Society. **44** (1), 544, **2024**.
24. HADDAD K., JELLALI S., JEGUIRIM M., BEN HASSEN TRABELSI A., LIMOUSY L. Investigations on phosphorus recovery from aqueous solutions by biochars derived from magnesium-pretreated cypress sawdust. Journal of Environmental Management. **216**, 305, **2 018**.
25. TIE J., LI W., DUAN X., WANG H., LIU S., ZHAO W. Magnetic iron-based waterworks sludge modified by chitosan and FeS for aqueous Cr(VI) adsorption and reduction. RSC Advances. **14** (39), 28915, **2024**.
26. DOMINGUEZ M., JEAMILETTE M., AND UEROA K. Adsorption of methylene blue dye using common walnut shell (Juglans regia) like biosorbent: implications for wastewater treatment. Green Chemistry Letters and Reviews. **17** (1), 2362257, **2024**.
27. LI Z., WEI Y., WU H., YUAN P., BU H., TAN X. Efficient and sustainable phosphate removal and recovery from wastewater with zinc-substituted magnetite. Separation and Purification Technology. **360**, 130642, **2025**.
28. SUN W., LIU C., LIU S., ZHANG J., CHEN H., QIU Z. Effective adsorption of Congo red by an innovative biochar/LDH-derived MIL-100(Al): Investigation of coexisting pollutants and mechanism revelation. Separation and Purification Technology. **359**, 130670, **2025**.
29. HART J.N., MAY P.W., ALLAN N.L., HALLAM K.R., CLAEYSSENS F., FUGE G.M., RUDA M., HEARD P.J. Towards new binary compounds: synthesis of amorphous phosphorus carbide by pulsed laser deposition. Journal of Solid State Chemistry. **198**, 466, **2013**.
30. WANG C., ZHOU H., WANG Q., XU B., ZHU G. Efficiency and mechanism of phosphate adsorption and desorption of a novel Mg-loaded biochar material. Environmental Science and Pollution Research. **31** (3), 4425, **2024**.
31. CHUBAR N. XPS determined mechanism of selenite ($HSeO^{3-}$) sorption in absence/presence of sulfate (SO_4^{2-}) on Mg-Al-CO_3 Layered double hydroxides (LDHs): Solid phase speciation focus. Journal of Environmental Chemical Engineering. **11** (3), 109669, **2023**.
32. CHEN J., LAN X., WANG C., ZHANG Q. The Formation Mechanism and Corrosion Resistance of a Composite Phosphate Conversion Film on AM60 Alloy. Materials. **11** (3), **2018**.
33. LIANG K.A., CHIH H.Y., LIU I.J., YEH N.T., HSU T.C., CHIN H.Y., TZANG B.S., CHIANG W.H. Tumor-targeted delivery of hyaluronic acid/polydopamine-coated Fe^{2+}-doped nano-scaled metal-organic frameworks with doxorubicin payload for glutathione depletion-amplified chemodynamic-chemo cancer therapy. Journal of Colloid and Interface Science. **677**, 400, **2025**.
34. CUI Q., XU J., WANG W., TAN L., CUI Y., WANG T., LI G., SHE D., ZHENG J. Phosphorus recovery by core-shell γ-Al_2O_3/Fe_3O_4 biochar composite from aqueous phosphate solutions. Science of The Total Environment. **729**, 138892, **2020**.
35. RIVEROS G., MENESES S., ESCOBAR S., GARÍN C., CHORNIK B. Electron transfer rates of alkyl-ferrocene molecules forming incomplete monolayer on silicon electrodes. Journal of the Chilean Chemical Society. **55**, **2010**.
36. LIN L., FANG W., LIANG Q., XING Y., SUN M., LUO H. Synthesis of Fe-doped sludge biochar from Fenton sludge for efficient activation of peroxymonosulfate in tetracycline hydrochloride degradation. Journal of Environmental Chemical Engineering. **12** (3), 112590, **2024**.
37. SEVERO F.F., DA SILVA L.S., MOSCÔSO J.S.C., SARFARAZ Q., RODRIGUES JÚNIOR L.F., LOPES A.F., MARZARI L.B., MOLIN G.D. Chemical and physical characterization of rice husk biochar and ashes and their iron adsorption capacity. SN Applied Sciences. **2** (7), 1286, **2020**.
38. QIN Y., WU X., HUANG Q., BEIYUAN J., WANG J., LIU J., YUAN W., NIE C., WANG H. Phosphate Removal Mechanisms in Aqueous Solutions by Three Different Fe-Modified Biochars. International Journal of Environmental Research and Public Health. **20** (1), 326, **2022**.